IEEE Access
Multidisciplinary | Rapid Review | Open Access Journal

Received May 3, 2018, accepted June 26, 2018, date of publication July 9, 2018, date of current version July 30, 2018.

Digital Object Identifier 10.1109/ACCESS.2018.2854189

Low Loss and Ultra Flat Rectangular Waveguide Harmonic Coupler

MOHAMED MAMDOUH M. ALI, (Student Member, IEEE), SHOUKRY I. SHAMS, (Member, IEEE), AND ABDEL-RAZIK SEBAK, (Life Member, IEEE)
Electrical and Computer Engineering Department, Concordia University, Montréal, QC H4B 1R6, Canada
Corresponding author: Mohamed Mamdouh M. Ali (mohamed.ali@ieee.org)

ABSTRACT Recently, communication networks are evolving dramatically to meet the human dynamic needs as well as provide the required support for the massive expansion in future applications. This fosters the research in the mm-wave components to create a new infrastructure for these applications. As a result, the electrical characteristics of the designed components in terms of the bandwidth and the linearity have to be evaluated in an accurate way. The linearity of the mm-wave components is evaluated through the assessment of the inter-modulation of these components, especially at the second harmonic band. In this paper, a −17-dB harmonic coupler is designed to pick a strong sample at the second harmonic, while suppressing the fundamental signal at the coupled port. A design procedure for the proposed harmonic coupler is presented and illustrated. The fabricated unit is silver plated to minimize the losses, where the measured coupling at the second harmonic band shows an excellent agreement with the simulated ones. In addition, the measured coupling level at the fundamental band is below −75 dB.

INDEX TERMS Harmonic couplers, inter-modulation characterization, flat coupling.

I. INTRODUCTION

Future communication is moving toward the utilization of mm-wave bands to provide extremely high data rates and cover the massive number of access points [1], [2]. These mm-wave bands will support the next generation of mobile communication as well as the future IOT applications [3], [4]. This encourages the research community to direct more effort in the field of mm-wave components analysis and design. Many articles in the literature discussed the implementation of different microwave components in mm-wave bands based on modern guiding structures [5]–[7]. Although these components had gone through a great development cycle, the designed components have to be characterized accurately before any deployment in the standard systems. This increases the need for various assessment and testing components to evaluate the performance of mm-wave components in terms of the electrical characteristics and the linearity [8], [9]. The linearity of the components can be evaluated through the measurements of the inter-modulation of each component. This can be performed using a special type of couplers called harmonic couplers.

Couplers, in general, are passive devices used to obtain flat samples of a specific signal within the operating bandwidth. The couplers can be divided into two categories based on the coupling level; strong coupling structures such as 3dB hybrid couplers [10]–[12] and weak coupling structures such as cross-guide couplers and loop couplers [13], [14]. Another classification is based on the implementation technology, where couplers can be implemented based on traditional guiding structures such as rectangular waveguides or based on modern guiding structures such as substrate integrated waveguides (SIW) and printed ridge gap waveguides (PRGW) [15], [16]. The harmonic coupler is a special type of couplers used to characterize the inter-modulation effect through sensing the second harmonic frequency component and suppress the fundamental component sample inside the secondary arm. Many couplers in the literature perform the opposite operation, where the coupling is flat within the fundamental band while the harmonic signals were suppressed [17]–[19]. On the other hand, a few articles were intersected to couple the second harmonic band. However, most of these works were directed to the harvesting application rather the inter-modulation assessment [20], where the coupling flatness is not a critical parameter.

In this work, a low loss harmonic coupler is designed and tested showing superior electrical characteristics, where the losses are minimized through the silver plating. The coupling level has a mean value of −17dB with less than ±1dB of variation within the required bandwidth. This is achieved using multi-section coupling hole structure between both

coupling arms. The coupling of the fundamental signal is suppressed to be less than −75dB to have an excellent isolation. The presented coupler is considered as a weak coupling structure and it is implemented based on rectangular waveguide technology. This paper is organized as follows: Section II describes the general configuration of the presented coupler as well as the required specifications. Afterwards, the mathematical formulation is illustrated in details in Section III. In Section IV, the validation process of the proposed design procedure is discussed, where the fabricated prototype is measured in both the fundamental and the second harmonic band. Finally, the paper outcomes are summarized in Section V, where the future expansion of this work is proposed.

II. PROPOSED HARMONIC COUPLER SPECIFICATIONS

This work is done through collaboration with Scientific Microwave Corporation (SMC), where it is an R&D project to build up an inter-modulation test setup for mm-wave components. According to the system requirements, the fundamental frequency band is located in a Ka-band, specifically 37.5-39.5 GHz, while the second harmonic frequency band is 75-79 GHz. The required coupling level is −17 dB at the second harmonic band. The suppression of the fundamental band should exceed 65 dB. Regarding the component interface, it is specified as follows: The input and output of the main arm comply with a WR22 cover flange, while the output of the second arm is WR10. The directivity should be higher than 25 dB for the second harmonic band.

The geometrical configuration of the proposed coupler is shown in Figure 1(a). The proposed coupler consists of three main parts. The first part is the coupling section, which is a dissimilar multi-hole directional coupler with a primary arm of the WR19 waveguide, while the secondary arm is WR12 as shown in Figure 1(b). These standards are chosen to allow a smooth transition between the input and the output waveguide standard, these standards are WR22 and WR10 respectively, as mentioned before. The second part is a transition from WR22 to WR19 in the main arm and a transition from WR12 to WR10 for the secondary arm. The third part is a WR12 matched load, which is placed to terminate the secondary arm from one direction.

Therefore, the proposed harmonic coupler is designed through four steps; starting by designing the coupling section shown in Figure 1(b) to achieved a −17 dB coupling with a directivity beyond 25 dB. The second step is to provide a design for WR22 to WR19 multi-section transition with a deep matching level. The third step focus on the design of WR12-WR10 transition with 90° bend. Finally, the assembly of all the previous parts together as well as the validation of the proposed harmonic coupler through the measurement. It is worth mentioning that the design based on this scheme will result in a self-suppression of the fundamental signal inside the secondary arm as the fundamental signal will be an evanescent wave inside the secondary arm structure. Hence, the design effort will be directed to achieve both the coupling

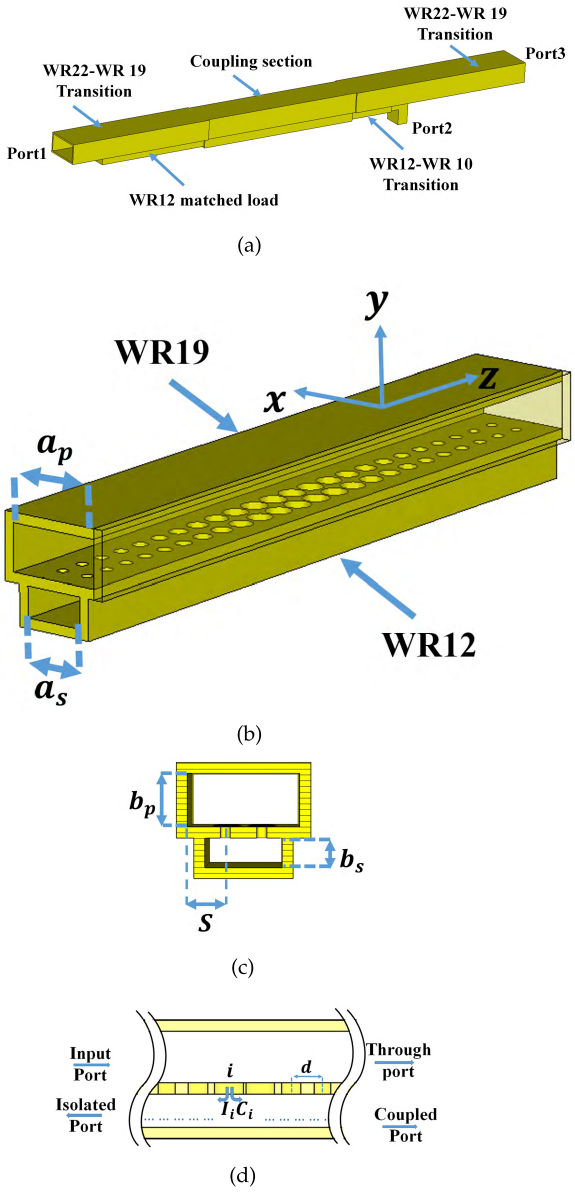

FIGURE 1. (a) The geometrical confiuration of proposed harmonic coupler (b) Coupling section. (c) Coupling section front view. (d) Coupling section side view.

flatness and the required directivity level at the second harmonic band.

III. MATHEMATICAL FORMULATION

A. COUPLING STRUCTURE ANALYSIS

The harmonic coupler coupling section consists of two dissimilar rectangular waveguides sharing a common broad wall. Both waveguides are coupled to each other through two rows of multihole with radius r and spaced $d = \lambda_{go}/4$ apart, where λ_{go} is the guided wavelength at the center frequency of operation. These rows are symmetrically located on the axial at a distance S from each side wall of the primary arm as shown in Figure 1(c) and 1(d).

Assuming the cross-sectional dimensions of the primary and secondary waveguides to be $a_p \times b_p$ and $a_s \times b_s$,

respectively. The incident TE_{10} mode with amplitude A is applied at the input port produces both electric and magnetic fields that can be written as [21]:

$$\vec{E} = \vec{y}A sin(k_{cp}x)e^{-j\beta_p z} \quad (1)$$

$$\vec{H} = AY_{10p}\left[-\vec{x}sin(k_{cp}x) + \vec{z}\frac{jk_{cp}}{\beta_p}cos(k_{cp}x)\right]e^{-j\beta_p z} \quad (2)$$

where $k_{cp} = \frac{\pi}{a_p}$, $\beta_p = \sqrt{k^2 - k_{cp}^2}$, and $Y_{10p} = \frac{\beta_p}{\omega\mu_o}$ are the phase constant, cutoff wave number, and wave admittance for the primary arm, respectively. Each aperture can be represented by an infinitesimal electric and magnetic polarization currents at the center of the aperture ($x = S$, $y = 0$). The z-dependence is neglected at this step, while it will be considered through the summation of the radiated wave along the holes. These polarization currents are related by the electric and magnetic current sources, J and M, respectively as follow:

$$\vec{J} = \vec{y}j\omega\varepsilon_o\alpha_e A \sin(k_{cp}S) \quad (3)$$

$$\vec{M} = j\omega\alpha_m AY_{10p}\left[\vec{x}\sin(k_{cp}S) + \vec{z} - j\frac{jk_{cp}}{\beta_p}\cos(k_{cp}S)\right] \quad (4)$$

where, $\alpha_e = \frac{2}{3}r^3\ CF_E$ and $\alpha_m = \frac{4}{3}r^3\ CF_M$ are the electric and magnetic polarizabilities of the round-slot, while CF_E and CF_M are the electric and magnetic polarizability correction factors which can be written for a circular coupling hole of radius r and thickness t as follow [21]–[27]:

$$CF_E = exp\left[\frac{-2\pi A_e t}{\lambda_{c1}}\sqrt{1 - \frac{\lambda_{c1}^2}{\lambda^2}}\right] \quad (5)$$

$$CF_M = exp\left[\frac{-2\pi A_m t}{\lambda_{c2}}\sqrt{1 - \frac{\lambda_{c2}^2}{\lambda^2}}\right] \quad (6)$$

where $\lambda_{c1} = 2.613\ r$ and $\lambda_{c2} = 3.412\ r$ are the cutoff wavelengths for the TM_{01} and TE_{11} modes of aperture waveguides, respectively, while A_e and A_m are effective wall thickness coefficients which have empirical equations listed in [26] and [27].

The forward and reverse waves radiated by the equivalent electric current J into the secondary waveguide of ith hole are given by [21], [27] :

$$C_{E,i}^{+} = C_{E,i}^{-} = A\frac{-jk^2}{a_s b_s \beta_s}\alpha_{e,i}\sin(k_{cp}S)\sin(k_{cs}S) \quad (7)$$

while, the forward and reverse waves radiated by the equivalent magnetic current M into the secondary waveguide of ith hole are given by [21], [27]:

$$C_{H,i}^{+} = jA\left[\alpha_{m,i}\frac{k_{cp}k_{cs}}{a_s b_s \beta_s}\cos(k_{cp}S)\cos(k_{cs}S) + \alpha_{m,i}\frac{\beta_p}{a_s b_s}\sin(k_{cp}S)\sin(k_{cs}S)\right] \quad (8)$$

$$C_{H,i}^{-} = jA\left[\alpha_{m,i}\frac{k_{cp}k_{cs}}{a_s b_s \beta_s}\cos(k_{cp}S)\cos(k_{cs}S) - \alpha_{m,i}\frac{\beta_p}{a_s b_s}\sin(k_{cp}S)\sin(k_{cs}S)\right] \quad (9)$$

where $k_{cs} = \frac{\pi}{a_s}$, $\beta_s = \sqrt{k^2 - k_{cs}^2}$, and $Y_{10s} = \frac{\beta_s}{\omega\mu_o}$ are the phase constant, cutoff wave number, and wave admittance for the secondary arm, respectively. Since the polarizabilities $\alpha_{e,i}, \alpha_{m,i}$ of ith hole are proportional to r_i^3, the coupling C_i and isolation I_i coefficients in the secondary guide of ith hole are given as:

$$C_i = C_{E,i}^{+} + C_{H,i}^{+} = K_f r_i^3 \quad (10)$$

$$I_i = C_{E,i}^{-} + C_{H,i}^{-} = K_b r_i^3 \quad (11)$$

where, K_f and K_b are constants for the coupling and isolation coefficients which can be written as:

$$K_f = jA\left[CF_M\frac{4k_{cp}k_{cs}}{3a_s b_s \beta_s}\cos(k_{cp}S)\cos(k_{cs}S) + (CF_M\frac{4\beta_p}{3a_s b_s} - CF_E\frac{2k^2}{3a_s b_s \beta_s})\sin(k_{cp}S)\sin(k_{cs}S)\right] \quad (12)$$

$$K_b = jA\left[CF_M\frac{4k_{cp}k_{cs}}{3a_s b_s \beta_s}\cos(k_{cp}S)\cos(k_{cs}S) - (CF_M\frac{4\beta_p}{3a_s b_s} + CF_E M\frac{2k^2}{3a_s b_s \beta_s})\sin(k_{cp}S)\sin(k_{cs}S)\right] \quad (13)$$

Therefore, the amplitude of the forward wave C and backward wave I for double rows of N holes can be written as

$$C = 2e^{-j\theta_s N}\sum_{i=0}^{N} K_f r_i^3 e^{-2j\theta_{Diff} i} \quad (14)$$

$$I = 2\sum_{i=0}^{N} K_b r_i^3 e^{-2j\theta_{Sum} i} \quad (15)$$

where $\theta_p = \beta_p d$ and $\theta_s = \beta_s d$, while $\theta_{Diff} = \frac{\theta_p - \theta_s}{2}$ and $\theta_{Sum} = \frac{\theta_s + \theta_p}{2}$.

B. MULTIHOLE COUPLING SECTION DESIGN PROCEDURE

The design of the coupling section starts with calculating the radius of the coupling apertures r_i $(i = 0, 1, .., N)$ to obtain a maximally flat response for the coupling as a stable coupling level is required. This can be achieved by equating the coupling coefficients with the binomial coefficients as $r_i^3 = KP(N, i)$, where K is a constant to be determined, and $P(N, i) = \frac{N!}{(N-i)!i!}$ are the binomial coefficients for i^{th} hole. Hence, the coupling and isolation coefficients of (14) and (15) can be written as follow:

$$C_{dB} = -20log\mid 2K_f K\mid -20log\mid \sum_{i=0}^{N} P(N, i)e^{-2j\theta_{Diff} i}\mid$$
$$= -20log\mid 2K_f K\mid -6N - 20log\mid \cos(\theta_{Diff})\mid^N \quad (16)$$

$$I_{dB} = -20log\mid 2K_b K\mid -20log\mid \sum_{i=0}^{N} P(N, i)e^{-2j\theta_{Sum} i}\mid$$
$$= -20log\mid 2K_b K\mid -6N - 20log\mid \cos(\theta_{Sum})\mid^N \quad (17)$$

The constant K is calculated to achieve the required coupling level value as well as to determine the radius of the

TABLE 1. Final dimensions of the coupling section (mm).

Dimension	Value	Dimension	Value
hole$_1$ (r_0)	0.25	hole$_6$ (r_5)	0.57
hole$_2$ (r_1)	0.27	hole$_7$ (r_6)	0.6
hole$_3$ (r_2)	0.34	hole$_8$ (r_7)	0.6
hole$_4$ (r_3)	0.47	hole$_9$ (r_8)	0.61
hole$_5$ (r_4)	0.53		

coupling holes, while the number of holes $N+1$ is calculated to satisfied the minimum directivity required. Hence, the directivity can be given as follow:

$$D_{dB} = -C_{dB} - I_{dB} \tag{18}$$

$$= 20log \mid \frac{K_f}{K_b} \mid + 20log \mid \frac{\cos(\theta_D)}{\cos(\theta_S)} \mid^N \tag{19}$$

Since the term $log \mid \frac{K_f}{K_b} \mid$ has a slight dependency on frequency and can be neglected compared to the second term, we can assume that the minimum directivity D_{dBmin} over the frequency band of operation is controlled by the second term and can be written as:

$$D_{dBmin} = 20log \mid \frac{\cos(\theta_D)}{\cos(\theta_S)} \mid^N \tag{20}$$

Hence, the minimum value of N to satisfy the minimum directivity D_{dBmin} over the frequency band can be calculated using (20). Substituting in (16) by the desired coupling, the value of the constant K can be calculated. Then, by knowing the constant K and the number of holes N, the radius of holes having a binomial distribution can be calculated. Increasing the number of holes will not only satisfy a high directivity, but also results in a feasible holes edge to edge spacing among the holes. This should be taken in consideration since relatively strong coupling is required which results in either large hole diameters or large number of holes.

Based on the design procedure discussed before, the number of holes $(N+1) = 18$ is selected to achieve a -17 dB coupling as well as a directivity more than 25 dB over the operating frequency band. This results in initial holes diameter values based on binomial distribution. These coupling holes are spaced a distance $d = \lambda_{gs}/4$ apart, where λ_{gs} is the guided wavelength at the center frequency of operation in the secondary waveguide. These holes are initially symmetrically located on the axial at a distance $S = a_s/4$. Further tuning is performed a round 5% to adjust the coupling level since the wall thickness $T = 0.508\ mm$ is considered in the fabrication process as well as the simulation. The optimum holes dimensions are located at a distance $S = 1.61036\ mm$ and spacing $d = 1.524\ mm$, where Table 1 indicates the final dimensions for the coupling holes. Both the coupling coefficient and the directivity will be compared with the analytic model and the measured results in the validation and experimental results section.

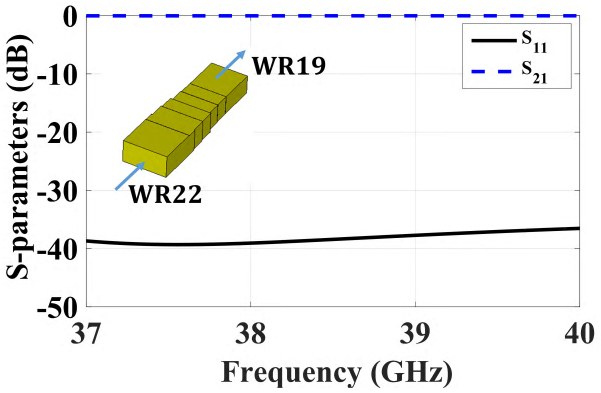

FIGURE 2. Multisection transition between a lower and a higher band waveguide.

C. MULTISECTION WAVEGUIDE TRANSITION DESIGN

The design procedure of waveguide transition is presented in this section using multisection transformer shown in Figure 2. Many articles have discussed the design of transitions between two waveguides operating in different frequency bands [28]–[31]. The proposed transition consists of M equal-length sections of waveguides with length L_i having a cross-sections of $a_i \times b_i$, where $i = 1, 2, \ldots, M$. This transition is connected between a lower and a higher band waveguides with cross-sections $a_l \times b_l$ and $a_h \times b_h$, respectively. The proposed transition is designed based on Chebyshev matching transformer which featured with wide bandwidth. The proposed transition should achieve a matching level beyond -30 dB (VSWR < 1.1) over the center frequency band. The fractional bandwidth of the transition is defined as [28]:

$$B.W = 2\frac{\lambda_{gh} - \lambda_{gl}}{\lambda_{gh} + \lambda_{gl}}, \tag{21}$$

where λ_{gl}, and λ_{gh} are the guided wavelength in a lower and a higher band waveguides at the center frequency. Hence, the length of wavegudie transformer sections is given as [28]:

$$L_i = \frac{\lambda_{gh}\lambda_{gl}}{2(\lambda_{gh} + \lambda_{gl})} \tag{22}$$

assuming impedance ratio $R = \frac{Z_h}{Z_l}$, where Z_h and Z_l are the characteristic impedances at the center frequency for a higher and a lower band waveguides, respectively. The characteristic impedances for a rectangular waveguide section can be given as [28]:

$$Z_{og} \simeq 600\frac{b}{a}\frac{\lambda_g}{\lambda} \tag{23}$$

where λ_g is the guided wavelength for a waveguide with cross-section $a \times b$ at the center frequency [31]. The number of steps required for a given maximum VSWR (V_r) can be roughly calculated by a trial and error solution of the following equation [28]:

$$heT_M^2\left[\frac{1}{sin(\pi B.W/4)}\right] = \frac{\xi_a}{\xi_r} \tag{24}$$

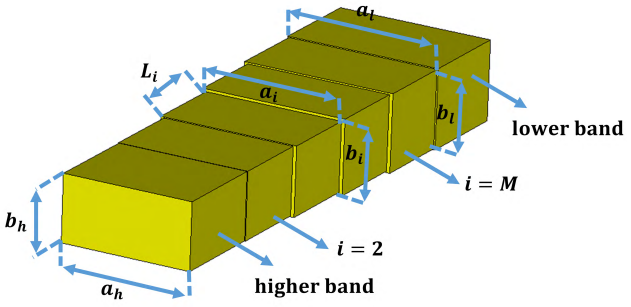

FIGURE 3. S-parameters of the primary arm transition.

where, $\xi_a = \frac{(R-1)^2}{4R}$ and $\xi_r = \frac{(V_r-1)^2}{4V_r}$. T_M is a Chebyshev polynomial of order M. Once the number of sections has been calculated, the Chebyshev reflection coefficients and associated characteristic impedancess for each section are calculated [21]. The cross-section dimensions $a_i \times b_i$ of each section are calculated using (23) by assuming $b_i = a_i/2$ as initial values.

The design procedure discussed before is used to design a double plane primary arm transition, where the lower and upper band waveguides are WR22 and WR19, respectively. The proposed transition should achieve a maximum VSWR $V_r = 1.1$ over the fundamental frequency of 38.5 GHz with a fractional bandwidth $B.W = 23\%$. From (24), the proposed transition must have at least three sections($M = 3$). The number of sections used for the proposed transition is ($M = 4$), where the final dimensions for the proposed transition are indicated in Table 2. All the simulations are performed using the electromagnetic (EM) computer simulation technology (CST) Microwave Studio Transient solver 2017. The accuracy is adjusted to be -40 dB and the meshing type is hexahedral with 20 cells per wavelength. The simulation S-parameter for the proposed transition is shown in Figure 3 which illustrates a matching level less than -30 dB over the fundamental frequency band.

TABLE 2. Final dimensions of the primary arm AND secondary arm transition in milimeter.

WG transition	WR22-WR19		WR12-WR10	
Transformer length	L_i	2	L_i	1
Section 1	a_1	4.8	a_1	2.6
	b_1	2.4	b_1	1.27
Section 2	a_2	4.9	a_2	2.6
	b_2	2.5	b_2	1.27
Section 3	a_3	5.3	a_3	2.8
	b_3	2.7	b_3	1.27
Section 4	a_4	5.5	a_4	3.1
	b_4	2.8	b_4	1.27

Based on the similar design procedure discussed before, a secondary arm transition is designed, where the lower and upper band waveguides are WR12 and WR10, respectively. Single plane transition are used since the height of lower band waveguide (WR12) is selected equal to the height of the higher band waveguide (WR10) since both standard heights are close to each other. The proposed transition should achieve a maximum VSWR $V_r = 1.1$ over the second harmonic frequency of 77 GHz with a fractional bandwidth $B.W = 6\%$. The number of sections used for the proposed transition is ($M = 4$), where the final dimensions for the proposed transition are indicated in Table 2. The simulation S-parameter for the proposed transition is shown in Figure 4 which illustrates a matching level less than -40 dB over the second harmonic frequency band.

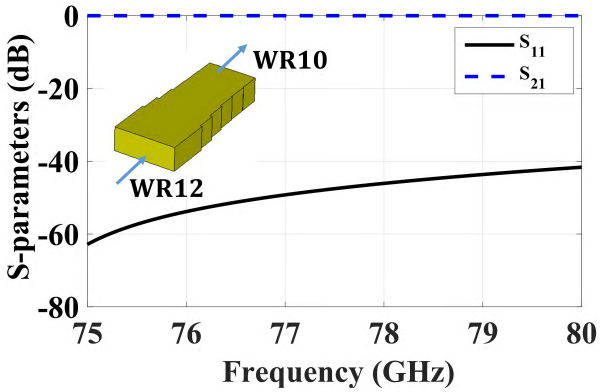

FIGURE 4. S-parameters of the secondary arm transition.

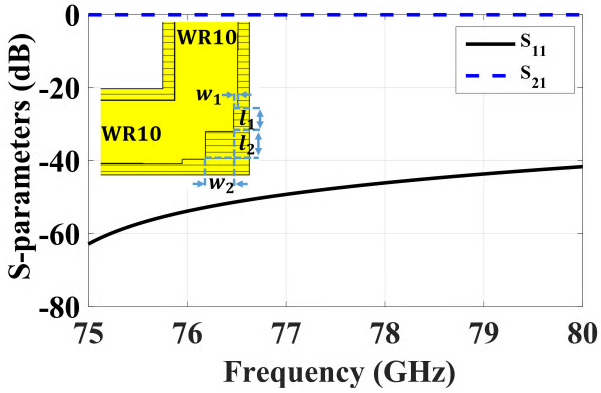

FIGURE 5. S-parameters of the secondary arm transition a 90° E-plane bend in WR10 waveguide standard.

A 90° E-plane bend is designed for WR10 waveguide standard in the secondary arm as shown in Figure 5. In order to achieve low return loss, three stairs are inserted to eliminate the discontinuity produced by the 90° edge as shown in Figure 5. These stairs have a dimension of $w_1 \times l_1 = 0.08 \times 0.46$ mm and $w_2 \times l_2 = 0.56 \times 0.56$ mm, while the third stair is the mirror of the first one. These dimensions are achieved through optimization process using CST simulator. The simulation S-parameter for the proposed bend is shown in Figure 5 which illustrates a low return loss less than -40 dB over the second harmonic frequency band. All the previous designed components are assembled together to construct the harmonic coupler shown in Figure 1(a),

where the simulated S-parameter will be compared with the measurement in the experimental and validation section.

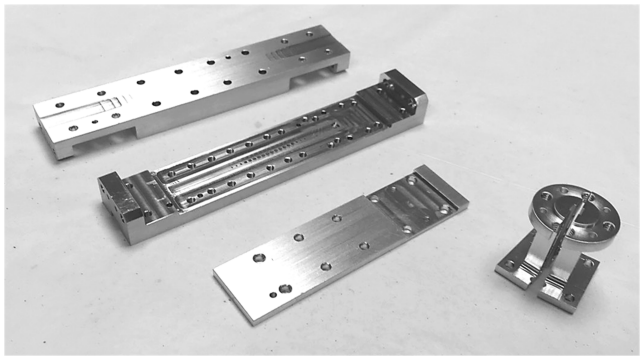

(a)

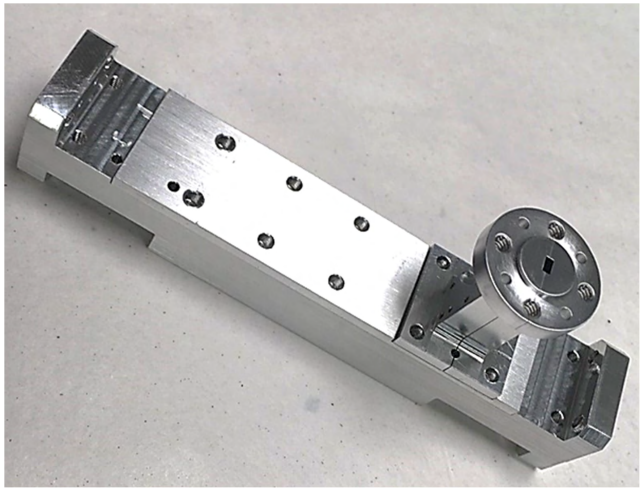

(b)

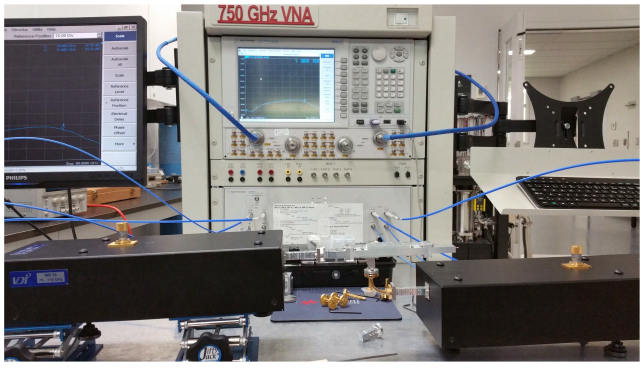

(c)

FIGURE 6. (a) The fabricated parts of the harmonic coupler. (b) Harmonic coupler after assembly (c) Measurement setup.

IV. VALIDATION AND EXPERIMENTAL RESULTS

The proposed harmonic coupler is fabricated using (MATSUURA MC-510VG) CNC machine, which has a tolerance of 0.0005 inches in all dimensions. The proposed device is fabricated using aluminum and silver painted to reduce the losses. Figure 6(a) show the fabricated parts of the proposed prototype. The proposed coupler parts are assembled and tested as shown in Figure 6(b) and 6(c). The measurement process is performed through measuring the proposed harmonic coupler in both the fundamental and second harmonic frequency bands. Through the measurement in the fundamental frequency band, WR10 to WR22 transition is used in the secondary arm to allow a double offset short calibration to calibrate the ANRITSU (MS46322A) VNA network analyzer. The coupling coefficient is measured in the fundamental frequency band, where the measured coupling level is less than −75 dB as shown in Figure 7(a).

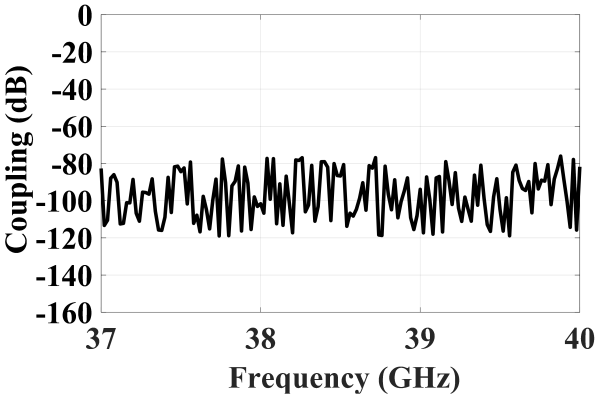

(d)

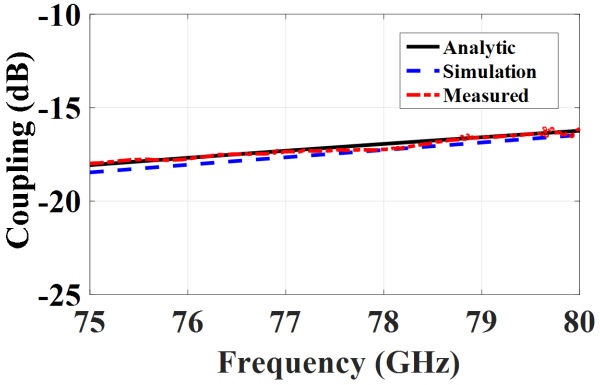

(e)

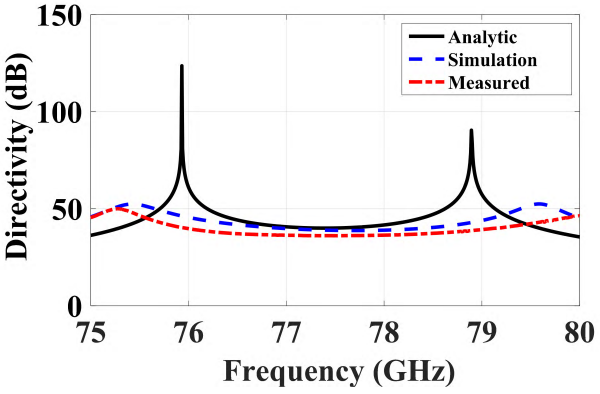

(f)

FIGURE 7. (d) Measured fundamental coupling level. Harmonic coupler comparison between simulations and measurement the second harmonic band: (e) Coupling, and (f) Directivity.

TABLE 3. Comparison between harmonic coupler configurations.

Reference	[20]	[20]	This work
Operating bands	Ku-band/ Ka-band	Ka-band/E-band	Q-band/E-band
Length	$\sim$ 5 inches	$\sim$ 3 inches	= 3.3 inches
Coupling flatness	High variation > $\pm$ 5 dB	High variation > $\pm$ 5 dB	Small variation = $\pm$0.75 dB
Application	Harvesting	Harvesting	Inter-modulation assessment

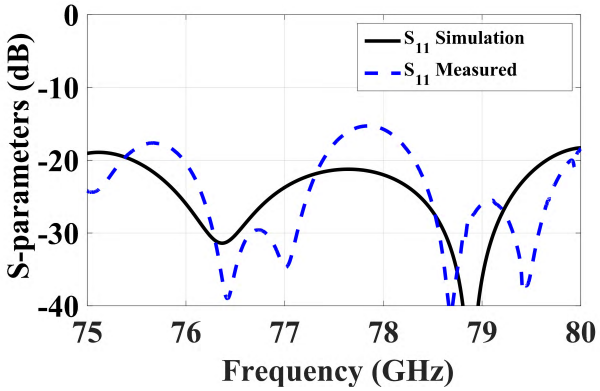

(g)

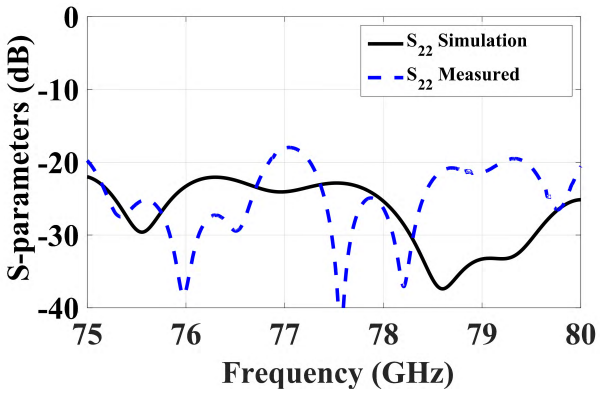

(h)

FIGURE 8. Harmonic coupler return loss comparison between simulations and measurement in the second harmonic band: (g) Main arm, and (h) Secondary arm.

Through the measurement of the second harmonic, two sections of WR22 to WR10 transition are used to allow a TRL calibration to calibrate the (N52271A) PNA network analyzer as shown in Figure 6(c). The fabricated prototype is tested using one of the states of art microwave equipment and facilities located at the Poly-Grames Research Center where the THz VNA up to 750 GHz is used to test the proposed device. The comparison between the measurement and the simulation as well as the analytic for both coupling and directivity are presented in Figure 7(b) and 7(c), respectively. Figure 7(b) shows an excellent agreement between the analytic and simulation as well as the measurement of the coupling coefficient, which demonstrates a coupling level of 17$\pm$ 0.75 dB. This agreement shows the validation of the proposed analytically model presented in Section III.

The measured directivity shown in Figure 7(c) demonstrates a directivity higher than 30 dB over the second harmonic frequency band with a good agreement between the simulation and analytic model. Although there is a clear discrepancy in the analytic directivity response compared to the simulated and measured, the proposed model shows the ability to provide accurate initial dimensions value for the harmonic coupler design. This discrepancy is due to the coupling between holes which is not considered in the analytical model. In addition, some approximations are used in the calculation of the coupling and directivity to provide simple and efficient design procedure.

The primary and secondary arms return loss are measured and compared with the simulation responses in Figure 8(a) and 8(b), respectively. It can be depicted from Figure 8(a) and 8(b) that the measured and the simulated return loss are in good agreement, where both achieve a return loss are less than -15 dB. The deviation between the measured and the simulated results are due to the using of another 90° through the measurement to allow the connection of the proposed device to the VNA analyzer equipment as shown in Figure 6(c).

Finally, the performance of the proposed harmonic coupler is compared with the performance of other structures in Table 3. The proposed harmonic coupler is designed to characterize the linearity of mm-wave components in Q and E bands through detection of second harmonic and suppression of first harmonic. Compared with the Ku/Ka-band and Ka/E-band harmonic couplers in [20], which having a large size and high coupling variation, the proposed coupler has a compact size of 3.3 inches with small coupling variation around $\pm$0.75 dB.

V. CONCLUSION

A silver plated harmonic coupler has been presented with $-$17dB flat coupling response. The measured coupling level variation is less than $\pm$1dB over the required operating bandwidth, while the directiveity exceeds 30dB within the same band. The introduced harmonic coupler has provided high suppression of the fundamental signal inside the secondary arm, beyond 76 dB, in order to isolate the second harmonic sample. In addition, a systematic design procedure has been illustrated to facilitate the reproduction of this kind of couplers for other applications. The final structure is fabricated of aluminum and silver painted, where the measured results are in a good agreement with the simulated ones. This work can be extended in future through applying the same design

procedure at different bands. The overall size can be minimized using a smaller number of holes or by utilizing different polynomial in obtaining the dimensions of the holes.

ACKNOWLEDGMENT

The authors would like to thank Professor Ke Wu for his support in measuring the proposed device using the advanced facilities in Poly-Grams Laboratory in Ecole Poly-Techniques.

REFERENCES

[1] M. Agiwal, A. Roy, and N. Saxena, "Next generation 5G wireless networks: A comprehensive survey," *IEEE Commun. Surveys Tuts.*, vol. 18, no. 3, pp. 1617–1655, 3rd Quart., 2016.

[2] T. S. Rappaport, J. N. Murdock, and F. Gutierrez, Jr., "State of the art in 60-GHz integrated circuits and systems for wireless communications," *Proc. IEEE*, vol. 99, no. 8, pp. 1390–1436, Aug. 2011.

[3] J.-J. DeLisle, "4 major M2M and IoT challenges you need to know," *Microw. RF*, vol. 54, no. 2, pp. 36–38, 2015.

[4] P. F. Freidl, M. E. Gadringer, D. Amschl, and W. Bcõsch, "mm-Wave RFID for IoT applications," in *Proc. Integr. Nonlinear Microw. Millimetre-Wave Circuits Workshop (INMMiC)*, Graz, Austria, 2017, pp. 1–3.

[5] M. A. Abdelaal, S. I. Shams, and A. A. Kishk, "90° phase shifter based on substrate integrated waveguide technology for Ku-band applications," in *Proc. 32nd Gen. Assem. Sci. Symp. Int. Union Radio*, 2017, pp. 1–3.

[6] S. I. Shams and A. A. Kishk, "Printed texture with triangle flat pins for bandwidth enhancement of the ridge gap waveguide," *IEEE Trans. Microw. Theory Techn.*, vol. 65, no. 6, pp. 2093–2100, Jun. 2017.

[7] S. I. Shams and A. A. Kishk, "Determining the stopband of a periodic bed of nails from the dispersion relation measurements prediction," *IEEE Trans. Compon., Packag. Manuf. Technol.*, vol. 7, no. 4, pp. 621–629, Apr. 2017.

[8] J. P. Teyssier, J. Sombrin, R. Quéré, S. Laurent, and F. Gizard, "A test set-up for the analysis of multi-tone intermodulation in microwave devices," in *Proc. 84th ARFTG Microw. Meas. Conf.*, Boulder, CO, USA, 2014, pp. 1–3.

[9] M. Marchetti, M. J. Pelk, K. Buisman, W. C. E. Neo, M. Spirito, and L. C. N. de Vreede, "Active harmonic load–pull with realistic wideband communications signals," *IEEE Trans. Microw. Theory Techn.*, vol. 56, no. 12, pp. 2979–2988, Dec. 2008.

[10] S.-C. Jung, R. Negra, and F. M. Ghannouchi, "A miniaturized double-stage 3 dB broadband branch-line hybrid coupler using distributed capacitors," in *Proc. Asia–Pacific Microw. Conf.*, Singapore, 2009, pp. 1323–1326.

[11] S. Y. Zheng, S. H. Yeung, W. S. Chan, and K. F. Man, "Broadband 3 dB hybrid coupler with flat coupling designed by jumping genes evolutionary algorithm," in *Proc. IEEE Int. Conf. Ind. Technol. (ICIT)*, Chengdu, China, Apr. 2008, pp. 1–5.

[12] Y. Zhang, Q. Wang, and H. Xin, "A compact 3 dB *E*-plane waveguide directional coupler with full bandwidth," *IEEE Microw. Wireless Compon. Lett.*, vol. 24, no. 4, pp. 227–229, Apr. 2014.

[13] H. C. Early, "A wide-band directional coupler for wave guide," *Proc. IRE*, vol. JPROC-34, no. 11, pp. 883–886, Nov. 1946.

[14] S. I. Shams, M. Elsaadany, G. Saad, and A. A. Kishk, "Compact wideband dual loop coupler with high power handling capability for radar applications," *IEEE Microw. Wireless Compon. Lett.*, vol. 27, no. 10, pp. 900–902, Oct. 2017.

[15] F. Parment, A. Ghiotto, T.-P. Vuong, J.-M. Duchamp, and K. Wu, "Broadband directional Moreno coupler for high-performance air-filled SIW-based substrate integrated systems," in *IEEE MTT-S Int. Microw. Symp. Dig.*, San Francisco, CA, USA, May 2016, pp. 1–3.

[16] M. M. M. Ali, S. I. Shams, and A.-R. Sebak, "Printed ridge gap waveguide 3-dB coupler: Analysis and design procedure," *IEEE Access*, vol. 6, pp. 8501–8509, 2018.

[17] S. Velan, M. Kanagasabai, J. K. Pakkathillam, and S. K. Palaniswamy, "Compact paper-substrate rat-race coupler deploying modified stepped impedance stub and interdigitated slot resonator for wide-band harmonic suppression," *IET Microw., Antennas Propag.*, vol. 10, no. 15, pp. 1667–1672, Oct. 2016.

[18] D. Dousset, J. Bornemann, M. Daigle, S. Claude, and K. Wu, "Broadband 100 GHz substrate-integrated waveguide couplers with irregularly shaped via holes for higher-order mode suppression," in *Proc. Eur. Microw. Conf.*, Amsterdam, The Netherlands, Nov. 2012, pp. 277–280.

[19] S. Bayaskar, D. Brahme, and K. Shambavi, "Compact rat race coupler with harmonic suppression using circular defected ground structure (CDGS)," in *Proc. Int. Conf. Global Trends Signal Process., Inf. Comput. Commun. (ICGTSPICC)*, Jalgaon, India, 2016, pp. 316–319.

[20] R. N. Simons and E. G. Wintucky, "Waveguide multimode directional coupler for harvesting harmonic power from the output of traveling-wave tube amplifiers," in *IEEE MTT-S Int. Microw. Symp. Dig.*, Honolulu, HI, USA, Jun. 2017, pp. 380–383.

[21] D. M. Pozar, *Microwave Engineering*, 4th ed. Hoboken, NJ, USA: Wiley, 2011.

[22] H. A. Bethe, "Theory of diffraction by small holes," *Phys. Rev. Lett.*, vol. 66, nos. 7–8, pp. 163–182, Oct. 1944.

[23] S. B. Cohn, "Determination of aperture parameters by electrolytic-tank measurements," *Proc. IRE*, vol. JPROC-39, no. 11, pp. 1416–1421, Nov. 1951.

[24] S. B. Cohn, "The electric polarizability of apertures of arbitrary shape," *Proc. IRE*, vol. JPROC-40, no. 9, pp. 1069–1071, Sep. 1952.

[25] S. B. Cohn, "Microwave coupling by large apertures," *Proc. IRE*, vol. JPROC-40, no. 6, pp. 696–699, Jun. 1952.

[26] N. A. McDonald, "Electric and magnetic coupling through small apertures in shield walls of any thickness," *IEEE Trans. Microw. Theory Techn.*, vol. MTT-20, no. 10, pp. 689–695, Oct. 1972.

[27] R. Levy, "Improved single and multiaperature waveguide coupling theory, including explanation of mutual interactions," *IEEE Trans. Microw. Theory Techn.*, vol. MTT-28, no. 4, pp. 331–338, Apr. 1980.

[28] G. L. Matthaei, L. Young, and E. M. T. Jones, *Microwave Filters, Impedance-Matching Networks, and Coupling Structures* (Artech Microwave Library). Norwood, MA, USA: Artech House, 1980.

[29] F. Arndt, U. Tucholke, and T. Wriedt, "Computer-optimized multisection transformers between rectangular waveguides of adjacent frequency bands (short papers)," *IEEE Trans. Microw. Theory Techn.*, vol. MTT-32, no. 11, pp. 1479–1484, Nov. 1984.

[30] S. B. Cohn, "Optimum design of stepped transmission-line transformers," *IRE Trans. Microw. Theory Techn.*, vol. 3, no. 3, pp. 16–20, Apr. 1955.

[31] E. S. Hensperger, "Broad-band stepped transformers from rectangular to double-ridged waveguide," *IRE Trans. Microw. Theory Techn.*, vol. 6, no. 3, pp. 311–314, Jul. 1958.

MOHAMED MAMDOUH M. ALI (S'15) received the B.Sc. (Hons.) and M.Sc. degrees in electronics and communications engineering from Assiut University, Egypt, in 2010 and 2013, respectively. He is currently pursuing the Ph.D. degree in electrical and computer engineering from Concordia University, Montréal, QC, Canada, in 2016. From 2010 to 2015, he was a Teaching and Research Assistant with the Department of Electronics and Communications Engineering, Assiut University. He was a Teaching and Research Assistant with Concordia University. His current research interests include microwave reciprocal/nonreciprocal design and analysis and antenna design.

SHOUKRY I. SHAMS (M'04) received the B.Sc. (Hons.) and M.Sc. degrees in electronics and communications engineering from Cairo University, Egypt, in 2004 and 2009, respectively. He received the Ph.D. degree in electrical and computer engineering from Concordia University, Montréal, QC, Canada, in 2016.

From 2005 to 2006, he served as a Teaching and Research Assistant with the Department of Electronics and Communications Engineering, Cairo University. From 2006 to 2012, he served as a Teaching and Research Assistant with the IET Department, German University in Cairo. From 2012 to 2016, he was a Teaching and Research Assistant with Concordia University. His research interests include microwave reciprocal/nonreciprocal design and analysis, high power microwave subsystems, and antenna design and material measurement.

Dr. Shams received the Faculty Certificate of Honor in 1999, the Distinction with Honor from Cairo University in 2004. He received the Concordia University Recruitment Award in 2012 and Concordia University Accelerator Award in 2016. He was the GUC-IEEE Student Branch Chair from 2010 to 2012.

ABDEL-RAZIK SEBAK (F'10–LM'18) received the B.Sc. degree (Hons.) in electrical engineering from Cairo University, Cairo, Egypt, in 1976, the B.Sc. degree in applied mathematics from Ein Shams University, Cairo, in 1978, and the M.Eng. and Ph.D. degrees in electrical engineering from the University of Manitoba, Winnipeg, MB, Canada, in 1982 and 1984, respectively. From 1984 to 1986, he was with Canadian Marconi Company involving in the design of microstrip phased array antennas. From 1987 to 2002, he was a Professor with the Department of Electronics and Communication Engineering, University of Manitoba. He is currently a Professor with the Department of Electrical and Computer Engineering, Concordia University, Montréal, QC, Canada. His research interests include phased array antennas, millimeter-wave antennas and imaging, computational electromagnetics, and interaction of EM waves with engineered materials and bio electromagnetics. He is a member of the Canadian National Committee of International Union of Radio Science Commission B. He was a recipient of the 2000 and 1992 University of Manitoba Merit Award for outstanding Teaching and Research, the 1994 Rh Award for Outstanding Contributions to Scholarship and Research, and the 1996 Faculty of Engineering Superior. He has served as the Chair of the IEEE Canada Awards and Recognition Committee from 2002 to 2004, and as the Technical Program Chair of the 2002 IEEE CCECE Conference and the 2006 URSIANTEM Symposium. He is the Technical Program Co-Chair for the 2015 IEEE ICUWB Conference.